THE JOURNAL OF BIOLOGICAL CHEMISTRY VOL. 287, NO. 37, pp. 31582–31595, September 7, 2012
Published in the U.S.A.

The Role of Capsid Maturation on Adenovirus Priming for Sequential Uncoating*[S]

Received for publication, June 8, 2012, and in revised form, July 11, 2012 Published, JBC Papers in Press, July 12, 2012, DOI 10.1074/jbc.M112.389957

Ana J. Pérez-Berná[‡1], Alvaro Ortega-Esteban[§2], Rosa Menéndez-Conejero[‡3], Dennis C. Winkler[¶], Margarita Menéndez[‖], Alasdair C. Steven[¶], S. Jane Flint[**], Pedro J. de Pablo[§], and Carmen San Martín[‡4]

From the [‡]Department of Macromolecular Structure, Centro Nacional de Biotecnología, and [§]Department of Physics of Condensed Matter, Universidad Autónoma de Madrid, 28049 Madrid, Spain, the [‖]Instituto de Química Física Rocasolano and CIBER de Enfermedades Respiratorias, 28006-Madrid, Spain, the [¶]Laboratory of Structural Biology, NIAMS, National Institutes of Health, Bethesda, Maryland 20892, and the [**]Department of Molecular Biology, Princeton University, Princeton, New Jersey 08544

Background: Adenovirus proteolytic maturation is required for correct uncoating in the cell.
Results: Maturation makes the virion metastable and facilitates penton and peripheral core protein release, as well as cooperative genome ejection.
Conclusion: Precursor proteins act as scaffolds favoring assembly. Maturation primes adenovirus for uncoating.
Significance: Identifying the molecular determinants of virus stability and uncoating is key to understanding the infectious cycle.

Adenovirus assembly concludes with proteolytic processing of several capsid and core proteins. Immature virions containing precursor proteins lack infectivity because they cannot properly uncoat, becoming trapped in early endosomes. Structural studies have shown that precursors increase the network of interactions maintaining virion integrity. Using different biophysical techniques to analyze capsid disruption *in vitro*, we show that immature virions are more stable than the mature ones under a variety of stress conditions and that maturation primes adenovirus for highly cooperative DNA release. Cryoelectron tomography reveals that under mildly acidic conditions mimicking the early endosome, mature virions release pentons and peripheral core contents. At higher stress levels, both mature and immature capsids crack open. The virus core is completely released from cracked capsids in mature virions, but it remains connected to shell fragments in the immature particle. The extra stability of immature adenovirus does not equate with greater rigidity, because in nanoindentation assays immature virions exhibit greater elasticity than the mature particles. Our results have implications for the role of proteolytic maturation in adenovirus assembly and uncoating. Precursor proteins favor assembly by establishing stable interactions with the appropriate curvature and preventing premature ejection of contents by tightly sealing the capsid vertices. Upon maturation, core organization is looser, particularly at the periphery, and interactions preserving capsid curvature are weakened. The capsid becomes brittle, and pentons are more easily released. Based on these results, we hypothesize that changes in core compaction during maturation may increase capsid internal pressure to trigger proper uncoating of adenovirus.

Adenovirus is a mild pathogen for humans but can become clinically relevant in immunocompromised patients, and it is widely examined as a therapeutic vector (1, 2). The large (~950 Å) nonenveloped, pseudo T = 25 icosahedral capsid is assembled from at least 11 different types of proteins. The general icosahedral architecture can be described as two different systems of tiles. Nine trimers of the major coat protein, hexon, form the central plate of each facet, known as the Group of Nine (GON).[5] The five peripentonal hexon trimers, together with the penton base, form the second tile system, known as Group of Six (GOS) (3). Trimeric fibers protrude from each vertex.

Minor coat proteins IIIa, VI, VIII, and IX are required for correct capsid assembly and occupy specific positions in the capsid (3). Polypeptide IX has an extended structure and forms a sort of hairnet on the outer surface of the virion, keeping together the hexon trimers in each GON and binding GONs to GONs across the icosahedral edges. Each GON is further stabilized by copies of polypeptide VIII located around the icosahedral 3-fold symmetry axis inside the capsid. Also on the inner capsid surface, the N-terminal domain of polypeptide IIIa mediates the interaction between penton base and the peripentonal hexons to keep each GOS together. Finally, IIIa and VIII cooperate to bind each GOS to its five surrounding GONs. The

* This work was supported, in whole or in part, by National Institutes of Health Grants GM037705 and AI1058172 (to S. J. F.). This work was also supported by Ministry of Science and Innovation of Spain Grants BFU2010-16382/BMC (to C. S. M.), MAT2008-02533, PIB2010US-00233, and FIS2011-29493 (to P. J. P.), FIS2010-10552-E and FIS2011-16090-E (to C. S. M. and P. J. P.), and BFU2009-10052 (to M. M.), and by Local Madrid Government Grant P2009/MAT-1467 (to P. J. P.).
[S] This article contains supplemental Figs. S1–S6, Table S1, and Movies S1–S7.
[1] Recipient of Juan de la Cierva Postdoctoral Contract JCI-2009-05187 from the Ministry of Science and Innovation of Spain and recipient of additional support from Spain CSIC Travel Grant PA1002892.
[2] Recipient of FPU predoctoral fellowship from the Ministry of Education of Spain.
[3] Recipient of Predoctoral Fellowship FI08/00035 from the Instituto de Salud Carlos III of Spain.
[4] To whom correspondence should be addressed: Centro Nacional de Biotecnología. Darwin 3, 28049-Madrid, Spain. Tel.: 34-91-5855450; Fax: 34-91-5854506; E-mail: carmen@cnb.csic.es.

[5] The abbreviations used are: GON, Group of Nine; DSC, differential scanning calorimetry; BIR, breakage/indentation ratio; GOS, Group of Six; AVP, adenovirus protease; vp, virus particles; PI, propidium iodide; AFM, atomic force microscopy; EF, extrinsic fluorescence; N, newton.

remaining minor capsid protein, polypeptide VI, could not be traced in this study, but it has been assigned to density within the internal cavity of each hexon trimer (4, 5). The adenovirus core contains a single copy of the dsDNA genome and over 25 MDa of protein, including four DNA-binding viral proteins: polypeptides V, VII, μ, and the terminal protein. A few copies of the adenovirus protease (AVP) are also packaged (6). The disposition of DNA and proteins in the core is unclear.

Adenovirus cell entry has been extensively studied using group C human adenoviruses; these are most commonly used for vector development, in particular the highly homologous types 5 (HAdV-5) and 2 (HAdV-2) (7, 8). Adenovirus uncoating in the cell proceeds in a stepwise manner (9). The virus starts to disassemble at the plasma membrane, where upon binding to its receptor some fibers are released (10), and the penton base undergoes a conformational change that might result in weakening its interactions with the rest of the capsid (11). The virus is then internalized, and disassembly continues in the early endosome with release of some internal components, such as minor coat proteins IIIa, VI, VIII, and core polypeptide V (9, 12). This is a crucial step for infection, as polypeptide VI plays the key role of altering the endosomal membrane to facilitate virus escape to the cytosol (13). The partially disassembled virion does not proceed to later stages of the endocytic pathway but escapes the early endosome (14). At this point there must be a certain degree of dsDNA exposure to initiate inflammatory responses (15), but the virion is still stable enough to survive transport along microtubules to the nuclear pore (16, 17). There, the final phase of uncoating takes place. Upon complete dismantling of the weakened capsid, the virus DNA, together with major core protein VII, enters the nucleus (18–21).

Correct adenovirus uncoating is tightly linked to maturation. Cleavage of several structural proteins by AVP is required to yield the mature infectious virion (22). Immature virions contain the precursor versions of coat proteins IIIa, VI, and VIII and of core proteins VII, μ, and terminal protein. An experimental model for immature adenovirus is the HAdV-2 *ts1* mutant (23). When grown at the nonpermissive temperature of 39 °C, HAdV-2 *ts1* does not package AVP (24) and produces capsids containing the unprocessed protein precursors. Viral genome packaging is unimpaired, but the virus is not infectious. It has been shown that the defect in infectivity is linked to a defect in uncoating. Immature *ts1* attaches to the host cell and follows the same internalization process as the wild-type (WT) virus but fails to escape the endosome and is recycled to the membrane or degraded in lysosomes (14, 25).

Cryo-EM structural studies showed that in the immature virus, the presence of uncleaved precursors reinforces the network of interactions holding the virion together at three levels. First, the virus core is more compact and stable due to the condensing action of unprocessed polypeptides pVII and pre-μ; second, a "molecular stitch" formed by pIIIa and pVIII underpins the boundary between GOS and GONs (5, 26); and third, there is a more ordered interaction between pVI and the inner cavity of each hexon in the capsid (4, 5). To further investigate how the presence of uncleaved precursors translates into a deficient uncoating phenotype, we have compared the *in vitro* stability and disassembly of *ts1* and WT virions under different types of stress: thermal, chemical, or mechanical. We report the differences between mature and immature virions and discuss their implications for assembly and uncoating.

EXPERIMENTAL PROCEDURES

Virus Production and Purification—We used as wild-type control for mature virions the E1-deleted HAdV-5 variant Ad5GL (27), propagated in HEK293 cells. Ad5GL is completely WT for all structural polypeptides. Immature virus was obtained by propagating the HAdV-2 *ts1* mutant in HeLa cells at 39.5 °C, as described (5). Particles were purified by equilibrium centrifugation in CsCl gradients, desalted on a Bio-Rad 10 DC column, and stored in 20 mM Hepes, pH 7.8, 150 mM NaCl plus 10% glycerol at −70 °C. Virus titers were 5×10^{12} virus particles (vp)/ml for Ad5GL, and 1×10^{13} vp/ml for *ts1*.

Differential Scanning Calorimetry—DSC measurements were performed using a Microcal VP-DSC instrument (Microcal, Inc., Northampton, MA) at a heating rate of 60 °C/h and under an extra constant pressure of 2 atm to prevent degassing during the scan. The VP-viewer package was used for data acquisition. Samples of WT and *ts1* at ~5–7 × 10^{12} vp/ml were dialyzed against 8 mM Na_2HPO_4, 2 mM KH_2PO_4, 150 mM NaCl, and 0.1 mM EDTA, pH 7.4. The reference cell was loaded with buffer from the last dialysis, which was also used to run the buffer-buffer baseline. Apparent excess heat capacity curves were obtained after subtraction of the buffer-buffer baseline from the experimental heat capacity profiles and division by hexon molar concentration.

The Origin-DSC software package (7.0 version) was used for data analysis. The excess heat capacity profiles were theoretically analyzed in terms of independent, irreversible two-state transitions ($N_i \rightarrow D_i$) according to Equation 1 (28),

$$\Delta Cp^{ex}(T) = \sum_{i=1}^{6} \frac{\Delta H_i^{app} E_i^{app}}{RT_{mi}^2} \times \exp\left(\frac{E_i^{app}(T - T_{mi})}{RT_{mi}^2}\right) \times \exp\left(-\exp\left(\frac{E_i^{app}(T - T_{mi})}{RT_{mi}^2}\right)\right) \quad \text{(Eq. 1)}$$

where ΔCp^{ex} (T) is the excess heat capacity value at temperature T; T_{mi} is the temperature of the maximum for transition i; ΔH_i^{app} and ΔE_i^{app} are the apparent calorimetric enthalpy change and the activation energy for the same transition, and R is the gas constant.

Fluorescence Spectroscopy—Extrinsic fluorescence spectra were obtained from virus preparations subject to different kinds of stress: high temperature, pyridine, or acidic pH. Mature and immature virus samples (5×10^{10} vp/ml) were incubated in different buffers, depending on the experiment. Thermal disruption experiments were carried out in 8 mM Na_2HPO_4, 2 mM KH_2PO_4, 150 mM NaCl, and 0.1 mM EDTA, pH 7.4. For pH disruption experiments, the sample was diluted and subsequently dialyzed overnight at 4 °C against buffers at the appropriate values of pH: HCl/KCl in the 1–2.5 pH range, citric acid/sodium citrate at pH 3–6, and Na_2HPO_4/KH_2PO_4 at pH range 6.5–7.5, always with 150 mM NaCl and 0.1 mM EDTA.

Fluorescence emission spectra were obtained employing a Hitachi Model F-2500 FL spectrophotometer equipped with a

Peltier temperature control device. 1 mM propidium iodide (PI) (Molecular Probes) was added to the sample that was then allowed to equilibrate for 5 min before data acquisition. Sample volumes of 0.150 ml were used in sealed quartz cuvettes. The sample was excited at 535 nm, and fluorescence emission was monitored from 580 to 700 nm, using excitation and emission slit widths of 8 nm. Raw spectra were corrected by subtraction of the PI spectrum at each tested condition. The ratio of PI fluorescence to the initial emission (I/I_0) at the maximum position ($\lambda_{max} = 607$ nm) ± S.E. for three independent experiments was plotted as a function of stress condition values. Fluorescence intensity changes were fitted to a sum of sigmoids using the Origin software package, according to Equation 2,

$$I/I_0 = A_1 + \frac{B_1 - A_1}{1 + \exp\left(\frac{C_1 - x}{C_1 D_1}\right)} + \sum_{i=2}^{n}\left(B_{i-1} + \frac{B_i - B_{i-1}}{1 + \exp\left(\frac{C_{i-1} - x}{C_i D_i}\right)}\right) \quad \text{(Eq. 2)}$$

where A_i and B_i are the lower and upper platform values for each sigmoid (notice that starting from the second sigmoid, the lower platform A_i is forced to coincide with the previous upper platform B_{i-1}); C_i is the transition midpoint; and D_i is the slope. The number of sigmoid curves in the summatory (up to $n = 3$) was the minimum necessary to fit the experimental curves, based on best R^2 values.

The fluorescence thermal-disruption curve was also fitted in terms of the model used to analyze the calorimetric curves using Equation 3,

$$I/I_0(T) = I_F - (I_F - 1) \times \sum_{i=1}^{3} f_i \times \exp\left(-\exp\left(\frac{E_i^{app}(T - T_{mi})}{RT_{mi}^2}\right)\right) \quad \text{(Eq. 3)}$$

where I_F is the final value of I/I_0, and f_i is the relative contribution of transition i to the total variation of PI fluorescence (29).

Negative Staining Electron Microscopy—For imaging of disassembly products, samples treated as described for fluorescence spectroscopy were adsorbed, at a concentration of 5×10^{11} vp/ml, onto glow-discharged, collodion/carbon-coated EM grids, negatively stained with 2% uranyl acetate, and observed in a Jeol 1200EX-II transmission electron microscope. Percentages of intact, damaged, and collapsed capsids were quantified by counting the number of particles of each type per micrograph. Error bars refer to differences between different micrographs.

Cryoelectron Tomography—Viral samples subject to different kinds of stress were mixed at a concentration of 1×10^{12} vp/ml with 10-nm colloidal gold particles (AURION, Wageningen, The Netherlands) and vitrified as described (30). A Tecnai-12 electron microscope (FEI, Hillsboro, OR) operating at 120 kV with a LaB6 source and equipped with an energy filter (GIF 2002; Gatan, Pleasanton, CA) was used to collect tilt series at ~4-μm underfocus, covering the range ±70° in 2° increments. The data were acquired using the SerialEM package (31), for a total dose of ~70–80 electrons/Å^2 per series. Images were recorded on a 2048 × 2048-pixel CCD camera (Gatan, Pleasanton, CA) at ×38,500 magnification (7.8 Å/pixel). Data were pre-processed and aligned using the IMOD software package (32), with gold particles as fiducial markers.

The final aligned tilt series were normalized and reconstructed using the simultaneous iterative reconstruction technique implemented in Tomo3D (33). Individual virus particles were extracted from tomograms using IMOD. Tomograms were denoised by 100 iterations of anisotropic nonlinear diffusion (34). The in-plane resolution of the full tomograms was in the 43–55-Å range, as estimated using the Bsoft program TOMORES (35).

Dihedral angles were measured from central slices of single virion tomograms using the angle measurement tool in Adobe Photoshop. A virion was considered to conserve fibers if at least one fiber was clearly visible in the denoised tomogram. The presence or absence of pentons was determined manually by observation of single virion tomogram slices after alignment with an icosahedral three-dimensional map as a reference, and comparison with model maps of full and pentonless virions. Radial profiles were calculated from average virus tomograms calculated after aligning each individual map with an icosahedral reference. Icosahedral symmetry was considered for alignment but not imposed in the final averaged map or in the individual aligned maps, except for supplemental Fig. S6. Alignment was carried out using maximum likelihood procedures for tomography as implemented in XMIPP (36, 37).

Nanoindentation Assays—Stocks of WT and *ts1* virus in HBS buffer (20 mM Hepes, 150 mM NaCl, pH 7.8) were diluted in a solution of $NiCl_2$ in HBS to obtain a final solution with 5 mM of Ni^{2+}, and adsorbed onto freshly cleaved Muscovite mica (V-1 quality). A drop of 20 μl of the final solution, containing virus particles at concentrations between 1.5 and 2×10^{12} vp/ml, was deposited on the substrate and incubated for 30 min at 4 °C before washing with 5 mM $NiCl_2$ in HBS. The AFM tip was prewetted with 30 μl of the same buffer. The mica was placed on the AFM sample holder and immersed in 500 μl of buffer. The AFM (Nanotec Electrónica S.L., Madrid, Spain) was operated in Jumping Mode Plus (38) in liquid using rectangular cantilevers RC800PSA and Biolevers (BL-AC40TS) (Olympus, Tokyo, Japan) with nominal spring constants of 0.05 and 0.03 N/m, respectively. Cantilever spring constants were routinely calibrated by using the Sader method (39). AFM exploration at forces of ~100 pN indicated a random population of virions on the mica surface.

Single virus particles were deformed by the AFM tip by performing individual indentation (force *versus* *z*-piezo displacement (*FZ*)) experiments. To ensure that the indentation is performed at the top of the virus, the virus shell is zoomed in continuously by reducing the *x-y* scanning size until the bump of the very top is under the whole piezo scan. Then a large force indentation was executed at the top of the particle. Finally, an image of the virus was taken to confirm its disruption. The maximum force applied during each indentation was high enough to

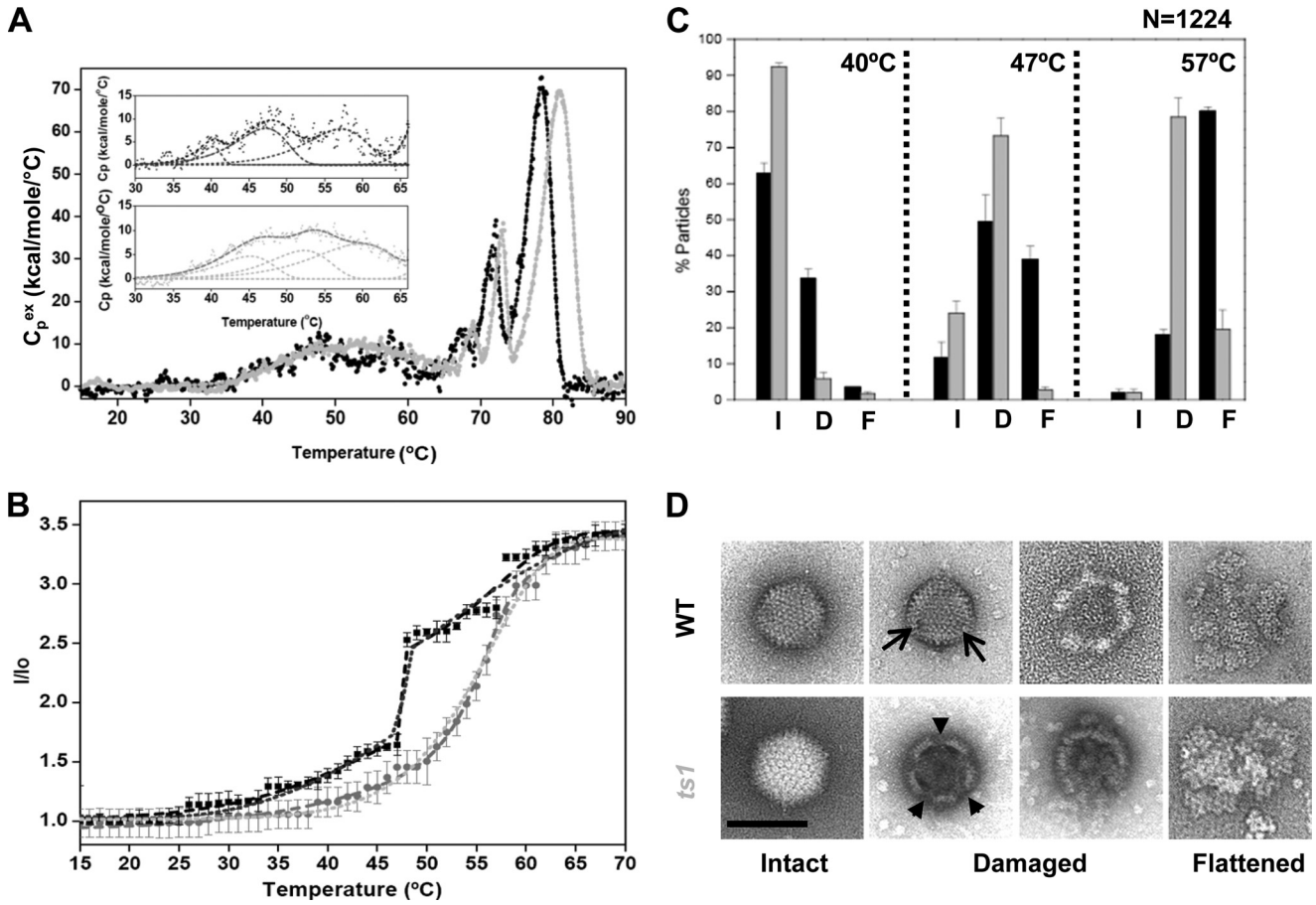

FIGURE 1. **Thermal capsid disruption.** *A,* thermograms showing WT and *ts1* thermally induced events upon virus heating at a constant rate of 60 °C/h (10 mM phosphate buffer, 150 mM NaCl, 0.1 mM EDTA, pH 7.4). The *solid line* is the theoretical fit of the experimental envelopes to irreversible two-state transitions using parameters given in Table 1. The *inset* shows the deconvolution of peaks likely corresponding to capsid disassembly. *B,* extrinsic fluorescence measurements showing DNA exposure to solvent upon heating. Average values and error bars corresponding to the standard deviation of three independent experiments are plotted. *Long dashed lines* correspond to the fit in terms of the model used for the calorimetric curves. *Short dashed lines* correspond to the fit according to a multiple sigmoid function. *C,* histogram showing structural effects of heating on the virus particles, as analyzed by negative staining. Categories are as follows: *I*, intact virions; *D*, damaged particles, including various degrees of disruption but retaining some degree of curvature; *F*, flattened capsids. *Error bars* indicate standard deviation in the particle counts between different micrographs. The total number of particles in the dataset, *N*, is indicated at the *top right corner*. *A–C*, *black symbols* and *lines* refer to WT virus; *gray symbols* and *lines* refer to *ts1*. *D,* gallery showing examples of intact, damaged, and flattened capsids. The *scale bar* corresponds to 100 nm. *Arrows* indicate missing vertex pentons; *arrowheads* indicate missing GOSs.

ensure that the virus particles are destroyed. The *FZ* speed is about 60 nm/s (40). Images were processed using the WSxM software (41).

RESULTS

Thermal Capsid Disruption—To directly detect the energy required to disrupt the capsid and to monitor the stability of the intermediates formed along the heat-induced disassembly process, DSC was used. DSC scans of mature (WT) and immature (*ts1*) adenovirus at physiological ionic strength and neutral pH are shown in Fig. 1*A*. As expected for a large, complex macromolecular specimen, thermal denaturation of both WT and *ts1* adenovirus was irreversible upon heating above 90 °C. Both thermograms show three well defined transitions (denoted as *T*2, *T*3, and *T*4 in Table 1) preceded by a broad endotherm between 36 and 65 °C in the *ts1* mutant and three discrete peaks in WT that extend over a similar range of temperature (Fig. 1*A*, *inset*). Indeed, deconvolution of the heat capacity profiles showed that the overall endotherm of both WT and *ts1* adenovirus can be described in terms of six irreversible two-state transitions whose apparent transition enthalpies, activation energies, and T_m values are summarized in Table 1.

The two last peaks of the thermograms (T_m values at 71.7 and 78.4 °C for WT and 72.8 and 81.0 °C for *ts1*) have previously been assigned to denaturation of the purified hexon protein (42), which is the most abundant component (>60%) of the protein shell. The minor transition (T_2) appearing at 67.3 °C for WT and 68.9 °C for *ts1* seems to be related to hexon stabilization upon GON formation, as it is absent in polypeptide IX-deleted recombinant viruses (42). The three low temperature transitions (denoted as T_{1A}, T_{1B}, and T_{1C} in Table 1) may correspond to capsid disassembly and reflect changes undergone by adenovirus during uncoating in the cell. However, whether they are directly due to disruption of hexon interactions or reflect denaturation of other virion components cannot at present be ascertained. All transitions occurred at higher temperatures for *ts1* than for WT, with differences in the 1–2 °C range for all T_m values except T_{1A} and T_{1B}, where differences were as high as 5 °C. These differences reveal an increased thermal stability of hexon and other virion structures in the immature capsid context.

TABLE 1
Thermal capsid disruption parameters from deconvolution of DSC endotherms

	T_{1A}			T_{1B}			T_{1C}		
	T_{m1A} (°C)	ΔH_{1A}^{app} (kcal/mol[1])	E_{1A}^{app} (kcal/mol)	T_{m1B} (°C)	ΔH_{1B}^{app} (kcal/mol)	E_{1B}^{app} (kcal/mol)	T_{m1C} (°C)	ΔH_{1C}^{app} (kcal/mol)	E_{1C}^{app} (kcal/mol)
WT	40.0 ± 0.3	12 ± 3	130 ± 30	47.4 ± 0.2	72 ± 8	61 ± 6	57.2 ± 0.3	83 ± 7	55 ± 6
ts1	45.2 ± 0.4	40 ± 10	57 ± 5	52.3 ± 0.7	60 ± 30	50 ± 10	60 ± 1	100 ± 30	40 ± 10

	T_2			T_3			T_4		
	T_{m2} (°C)	ΔH_2^{app} (kcal/mol)	E_2^{app} (kcal/mol)	T_{m3} (°C)	ΔH_3^{app} (kcal/mol)	E_3^{app} (kcal/mol)	T_{m4} (°C)	ΔH_4^{app} (kcal/mol)	E_4^{app} (kcal/mol)
WT	67.3 ± 0.1	36 ± 2	180 ± 10	71.7 ± 0.1	89 ± 2	219 ± 7	78.38 ± 0.01	312 ± 2	151 ± 1
ts1	68.9 ± 0.1	32 ± 2	250 ± 20	72.8 ± 0.1	72 ± 1	300 ± 5	80.95 ± 0.01	378 ± 2	125 ± 1

[1] ΔH units are kilocalories/mol of hexon monomer (720 hexon monomers/virion).

TABLE 2
EF analysis of thermal capsid disruption
Fitting of thermal disruption EF data to multiple sigmoid curves. Boldface indicates transitions with high cooperativity.

	WT		*ts1*	
	Midpoint	Slope	Midpoint	Slope
	°C		°C	
Sigmoid 1	38 ± 2	2.8 ± 0.5	41 ± 1	1.1 ± 0.1
Sigmoid 2	**48 ± 1**	**170 ± 10**	54 ± 1	8 ± 4
Sigmoid 3	58 ± 3	4 ± 1	65.0 ± 0.4	4.6 ± 0.6
R^2	0.99482		0.99483	

To define the conditions in which the particle undergoes partial disassembly and the DNA is exposed, we measured the DNA accessibility to solvent by using the DNA intercalating dye PI. PI fluorescence is quenched until the virus capsid is compromised and enhanced upon binding to DNA when it becomes accessible (43). As we have shown previously (5), similar degrees of DNA exposure occurred at higher temperatures for *ts1* than for WT (Fig. 1*B*). EF measurements were fitted to multiple sigmoidal curves with parameters shown in Table 2. WT presents a fluorescence burst at 47.5 °C. The sharp slope of the curve at this temperature indicates a highly cooperative process, also observed for WT forms of HAdV-2 and HAdV-5 at ~45 °C (5, 44, 45). In contrast, all transitions showed low cooperativity in *ts1*.

EF data were also analyzed using the irreversible transition model used for the DSC curves (Fig. 1*B*), and the best fitting parameters are compared with those derived from the heat capacity profiles in Table 3. The T_m values obtained from EF experiments for WT closely agreed with those deduced from DSC (Table 3), indicating that capsid protein denaturation (DSC) and DNA exposure (EF) events are correlated. Transition overlapping in the immature virus impaired a reliable analysis of the EF curve, as around 90% of the total emission variation can be apparently described by a single transition with a T_m value of 57.0 °C. Introduction of a third transition approached the T_m values to the DSC estimates but increased significantly the errors of the thermal parameters without improving the R^2 value.

Structural changes due to thermal disassembly were followed by EM. We had previously observed that WT capsids were completely disrupted and their contents released at 47 °C, whereas the *ts1* virion only lost vertex structures (pentons and peripentonal hexons, or GOS) and extruded part of its contents as a single nucleoprotein filament (5). Here, we report a quantitative description of capsid disruption patterns at different temperatures.

WT and *ts1* preparations were imaged by negative staining EM after heating at the temperatures corresponding to T_m values derived for WT. To interpret the EM observation, we grouped the observed particles into three categories (Fig. 1*C*): intact virions (**I**); damaged capsids, still retaining a spherical arrangement (**D**); and collapsed, flattened capsids (**F**). Fig. 1*D* shows examples of particles in the three categories (see also supplemental Fig. S1). At the T_{1A} transition temperature (40 °C), most *ts1* virions were intact, whereas a considerable proportion (~30%) of WT capsids showed small defects consistent with loss of pentons (Fig. 1*D*). The fact that the interior of these capsids does not appear dark indicates that they still contain stain-excluding material (protein/DNA), in agreement with the modest increase in DNA accessibility to PI indicated by EF. At the T_{1B} transition temperature (47 °C), only 10% of WT virions retained their structural integrity, with the rest showing different degrees of damage. In particular, about 40% of the WT virions appear as collapsed flat structures, with the icosahe-

TABLE 3
Comparison between capsid thermal disruption parameters obtained from DSC and calculated from EF spectroscopic curves using the same irreversible transition model

		T_{1A}			T_{1B}			T_{1C}		
		T_{m1A}	E_{1A}^{app}	f_{1A}	T_{m1B}	E_{1B}^{app}	f_{1B}	T_{m1C}	E_{1C}^{app}	f_{1C}
		℃	*kcal/mol*		℃	*kcal/mol*		℃	*kcal/mol*	
WT	DSC	40.0 ± 0.3	130 ± 30		47.4 ± 0.2	61 ± 6		57.2 ± 0.3	55 ± 6	
	Spectroscopy	40 ± 6	25 ± 10	0.23	47.8 ± 0.1	$>10^3$	0.30	57 ± 2	38 ± 10	0.47
ts1	DSC	45.1 ± 0.4	57 ± 5		52.3 ± 0.7	55 ± 10		60 ± 1	40 ± 10	
	Spectroscopy									
	$R^2 = 0.998$	(42 ± 40)	(21 ± 10)	(0.15)	(55.9 ± 0.4)	(90 ± 40)	(0.44)	(60 ± 10)	(40 ± 70)	(0.41)
	$R^2 = 0.997$	39 ± 3	39 ± 20	0.1	57.0 ± 0.2	48 ± 4	0.9			
	$R^2 = 0.996$				56.8 ± 0.2	40 ± 1	1.0			

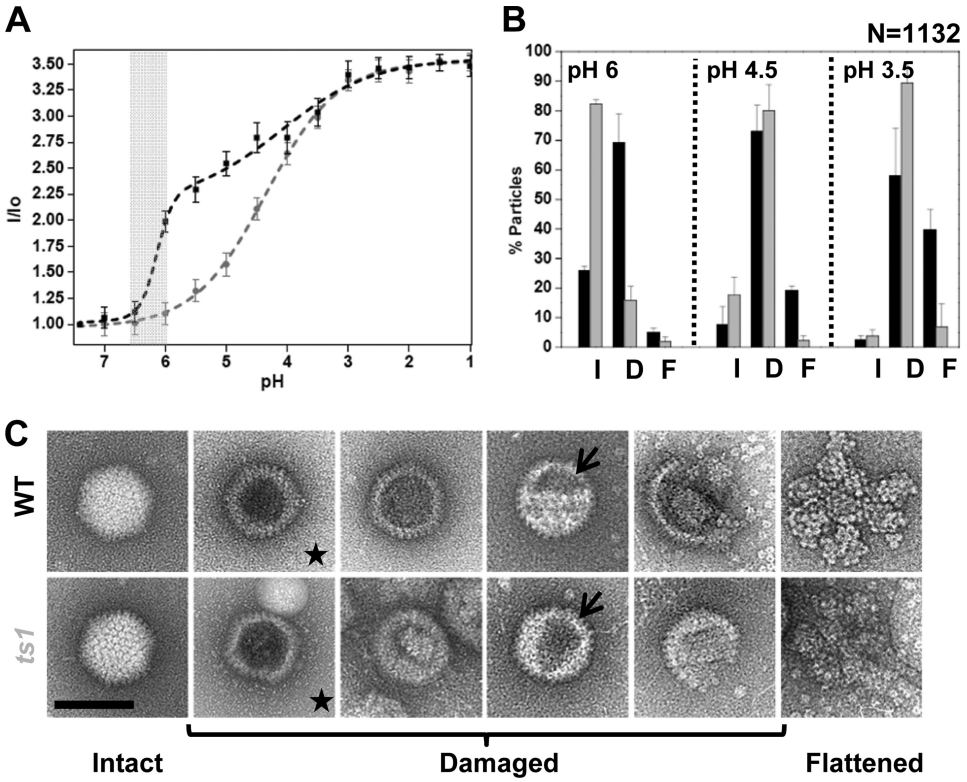

FIGURE 2. **Chemical capsid disruption: effect of acidification.** *A,* extrinsic fluorescence measurements showing DNA exposure to solvent upon acidification. Average values and *error bars* corresponding to the standard deviation of three experiments are plotted. *Dashed lines* correspond to the fit according to a multiple sigmoid function. The *shadowed area* indicates the pH range in the early endosome. *B,* histogram showing structural effects of acidification on the virus particles, as analyzed by negative staining. Categories are as follows: ***I***, intact virions; ***D***, damaged particles, including various degrees of disruption but retaining some degree of curvature; ***F***, flattened capsids. *Error bars* indicate standard deviation in the particle counts between different micrographs. The total number of particles in the dataset, *N*, is indicated at the *top right corner*. *A* and *B*, *black symbols* and *lines* refer to WT virus; *gray symbols* and *lines* refer to *ts1*. *C,* gallery showing examples of intact, damaged, and flattened capsids. Particles where the staining agent penetrates are indicated with a *star*. Particles lacking large capsid fragments are indicated with *arrows*. The *scale bar* corresponds to 100 nm.

drons split open, and large defects at the vertices consistent with loss of complete GOS. Immature *ts1* virions, however, are not flattened; they retain the capsid spherical arrangement although they have lost complete GOS. At 57 °C, the vast majority (~80%) of WT capsids are flattened, while most *ts1* virions still retain curvature, even when extensively damaged. Although capsid flattening is most likely an artifact induced by the negative staining preparation, the differences found between WT and *ts1* virions suggest that capsid precursors strengthen the seams at the icosahedral edges, preserving capsid curvature. At temperatures beyond 57 °C, only isolated capsomers or small capsid fragments are observed for both WT and *ts1*.

Chemical Capsid Disruption—Next, we subjected the adenovirus mature and immature capsids to different sources of chemical stress. Immature *ts1* virions showed higher stability than WT both in the presence of denaturant compounds and, most interestingly, upon acidification.

A critical point in adenovirus uncoating *in vivo* is acidification within the early endosome, where the luminal pH ranges between 6.5 and 6 (46). Upon acidification, the increase of PI fluorescence for WT, indicative of DNA accessibility, proceeds in a biphasic way (Fig. 2*A*). The first highly cooperative transition is centered at pH 6.1 and starts as the medium acidity approaches the endosomal range of pH (Table 4). In contrast, the immature virus withstood more severe values of pH (Fig.

TABLE 4

EF analysis of capsid disruption induced by acidification

Fitting of EF data to multiple sigmoid curves. Boldface indicates transitions with high cooperativity.

	WT		*ts1*	
	Midpoint (pH units)	Slope	Midpoint (pH units)	Slope
Sigmoid 1	**6.1 ± 0.1**	**48 ± 5**	4.4 ± 0.3	7.4 ± 0.3
Sigmoid 2	4.1 ± 0.4	5.4 ± 0.9		
R^2	0.99951		0.99916	

2*A*) and the *ts1* curve showed, apparently, only a broad transition centered at pH 4.1, which is near the midpoint of the second WT transition. At pH values below 3, both viruses present the same behavior. A highly cooperative transition leading to almost complete DNA exposure was also observed upon WT capsid disruption by the denaturant agent pyridine (supplemental Fig. S3 and supplemental Table S1).

EM analysis (Fig. 2*B* and supplemental Fig. S2) indicated that at pH 6 over 80% of the *ts1* particles were intact but more than 70% WT virions already showed damage. Again, complete collapse and flattening were rarely observed for *ts1* and WT. The same tendency regarding flattening was observed for disruption by pyridine (supplemental Fig. S3).

Acidification damage produced capsids with dark centers, indicating penetration of the staining agent. However, no evident gaps indicating loss of pentons were observed, meaning that the capsid defect allowing DNA exposure to PI and uranyl acetate is small and of low occurrence in the icosahedral network. Additionally, new kinds of disassembly intermediates were observed: particles with fissures and particles that had lost capsid fragments of different sizes and shapes ("chunks") but still retaining the polyhedral curvature (Fig. 2*C*). These kinds of images are consistent with the capsid releasing the stress imposed by acidification via cracks at hexameric positions, instead of by releasing vertex structures (47).

Interestingly, 74% of WT damaged particles at pH 6 (55% over total number of particles) were stain-filled capsids. In *ts1*, however, disruption via fissures and chunk release was more abundant: 56% (46% of the total) of *ts1* damaged particles corresponded to this category at pH 4.5, and 60% (58% of the total) at pH 3.5. This difference in disruption patterns suggests that the defect in the WT capsid that allows stain penetration is the physiological path for partial uncoating in the endosome, rather than the disruption via cracks. However, from the negative stain images, it was not clear exactly what this defect was, as no clear pattern of lost capsomers (*e.g.* vertices) was observed.

Cryoelectron Tomography of Disassembly Intermediates—DSC and EF provide bulk information on changes undergone by the specimen, but they do not reveal changes in individual virions. Imaging disassembled virions by negative stain provided single virion images; however, interaction with the carbon support and the acidic staining agent, plus drying and flattening, may result in additional changes not directly related to the stress conditions being tested. Furthermore, in negative stain images only a two-dimensional projection of the three-dimensional virion is obtained, and it is not possible to observe the internal structures of the particle. To obtain a better picture of the structural changes occurring during capsid disruption, we used cryoelectron tomography.

First, we investigated the changes in the structure of WT viruses at the stressor conditions where the first transition was observed in DSC or EF assays and where *ts1* virions remained mostly unaltered (Figs. 1–3 and supplemental Movies S1–S3): at 40 °C or pH 6.0. In both cases, tomograms showed that capsids conserved to a large extent their structural integrity, including attached fibers (Fig. 3*A* and supplemental Fig. S5). However, the aspect of the core differed between control and stressed viruses. In control conditions (25 °C, pH 7.4), the virion interior presented a smooth, flat density with gray levels similar to those of the capsid shell. In viruses incubated at pH 6, the core density appeared more heterogeneous and slightly weaker than that of the capsid. This same difference, sometimes more pronounced, was observed in the core of viruses heated at 40 °C. A radial average profile calculated from aligned individual virus tomograms indicated that, for both types of mild stress, the density of the outer region of the core was lower than in control viruses (Fig. 3*B*). This change in electron density is compatible with a relaxation of the DNA-protein complex or loss of peripheral core material. No decrease in core density was observed for *ts1* virions at pH 6 (supplemental Fig. S4).

Next, we searched for capsid defects that would account for the increase in DNA exposure observed in EF assays. Slice-by-slice analysis of individual virion tomograms indicated that both mild heating and acidification resulted in loss of pentons (Fig. 3*C* and supplemental Fig. S5). However, the degree of loss was different depending on the kind of stress; acidified viruses lost only one to two pentons, whereas heating produced the release of three to four pentons (Fig. 3*D*).

Concomitantly with a larger loss of pentons, fewer fibers were observed in heat-disrupted WT virions, although upon disruption at pH 6 more than 70% virions still conserved fibers (supplemental Fig. S5), *i.e.* mild acidification by itself is not causing massive fiber release. Occasionally, both at 40 °C or at pH 6, a short (25–30 nm long and 4–5 nm wide) stretch of DNA was seen to protrude out of the missing penton position (supplemental Fig. S6). However, this was an extremely rare event (less than 5% of analyzed viruses under mild stress conditions).

Tomograms of WT and *ts1* virions subject to high stress conditions (heating at 47 °C or acidification at pH 5; also pH 4 for *ts1*) were also obtained. At 47 °C, most WT virions appeared as empty broken shells with missing GOS (Fig. 4*A*, supplemental Fig. S5 and supplemental Movies S4 and S5). Only in a few cases some loose core structures remained attached to capsid fragments. Most immature *ts1* virions had also lost GOS and in some cases were cracked open; however, the core remained attached to cracked capsids and in a compacted state. We have previously reported that *ts1* virions disrupted at 47 °C extrude a nucleoprotein filament (5). However, no such filaments were observed in cryoelectron tomograms, although they are common occurrences in negative staining (5) or platinum/carbon shadowing preparations (data not shown). We conclude that filament extrusion is induced by the EM preparation conditions, namely a combination of adsorption to the support, staining with low pH uranyl salts or shadowing, and drying.

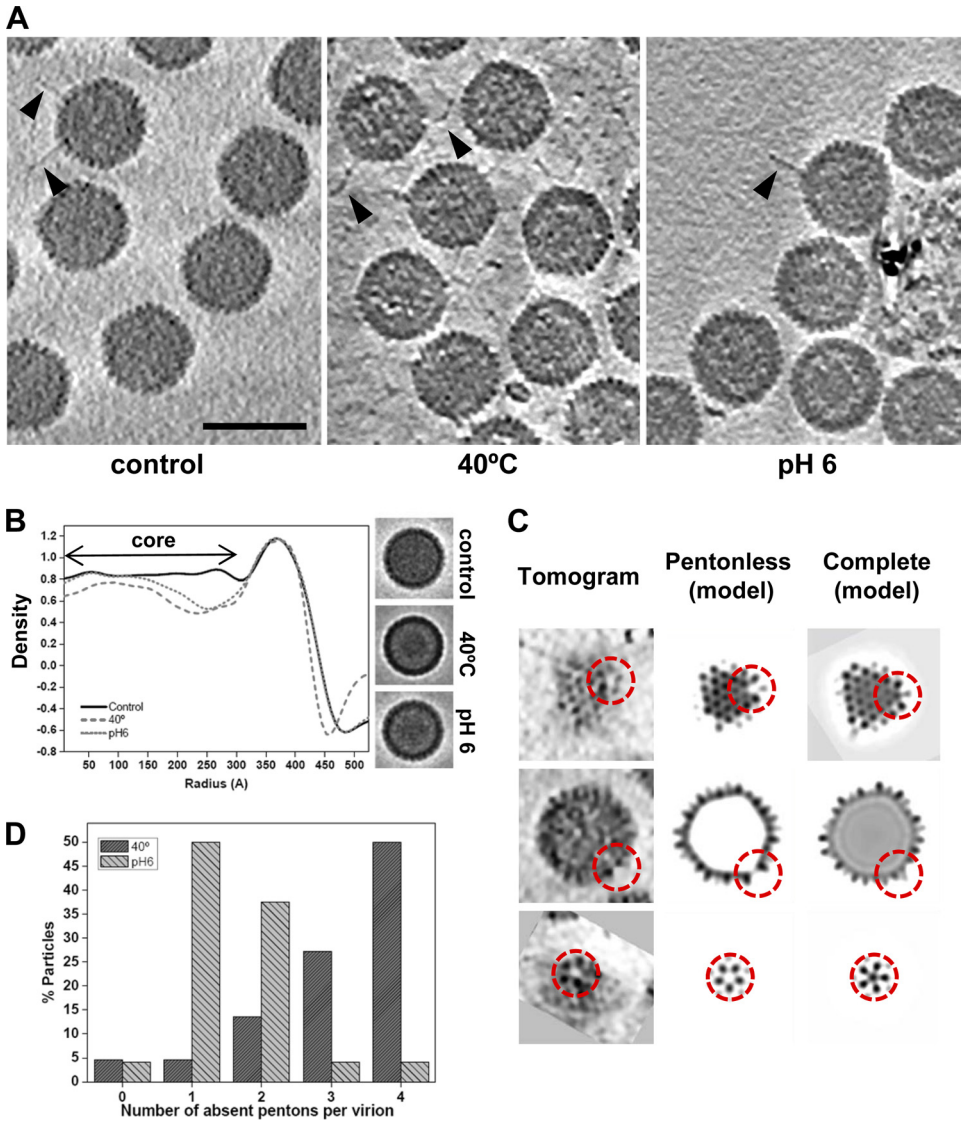

FIGURE 3. **Cryoelectron tomography analysis of structural changes induced by mild stress in WT adenovirus.** *A*, representative sections of tomograms showing WT virus in control conditions, 40 °C or pH 6, as indicated. The *bar* represents 100 nm. Some visible fibers are labeled with *arrowheads*. *B*, radial density profiles of average maps calculated from 22 individual virus tomograms for each case. The central section of each average map is shown at *right*. *C*, example sections of individual virus tomograms showing penton loss. Equivalent sections of a model lacking pentons, and of the full virion icosahedral map, are shown for comparison. Model maps are low pass-filtered at 50 Å resolution. *Red dashed circles* indicate the position of the vertex. *D*, histogram showing number of pentons lost per virion. No penton loss was observed in an equivalent dataset of control viruses. 33 individual virion tomograms (396 vertices) were analyzed for each condition.

A considerable proportion of *ts1* capsids remained intact at low pH values (more than 90% at pH 6 and up to 60% at pH 4; supplemental Fig. S5). Notably, fibers (which are not directly involved in proteolytic processing) remain attached to immature virions even under conditions as harsh as pH 4 (supplemental Fig. S5). Upon high acidification, WT shells had gaps consistent with loss of GOS and were only rarely seen in contact with any core remains. Conversely, *ts1* capsids only lost pentons and cracked open, whereas cores remained attached to shell fragments and in a condensed state (Fig. 4*B* and supplemental Movies S6 and S7).

Unlike for negative staining EM, no flattened capsids were observed in cryoelectron tomography images, confirming that flattening was a preparation artifact. However, measurement of dihedral angles in tomograms indicated that in high stress conditions the curvature of disrupted capsids departed from the icosahedral value (Table 5 and Fig. 4*C*) in both WT and *ts1* but with a more noticeable effect in WT. We conclude that flattened capsids observed by negative staining in WT correspond in solution to empty deformed capsids with reduced curvature reinforcements that become flat upon adsorption to carbon staining and drying. In *ts1*, loss of curvature is not so pronounced, and capsids are less prone to flattening during the negative staining procedure. Interestingly, curvature characteristics are preserved in *ts1* even in conditions where large vertex structures (GOS) are lost (47 °C). This observation suggests that the tighter interactions between capsid and compacted core established by precursor proteins play a role in determination and maintenance of capsid curvature during assembly.

For both WT and *ts1*, a small proportion of particles that appeared as intact capsids was found to lack some pentons after closer inspection (supplemental Fig. S5, class "P"). When these

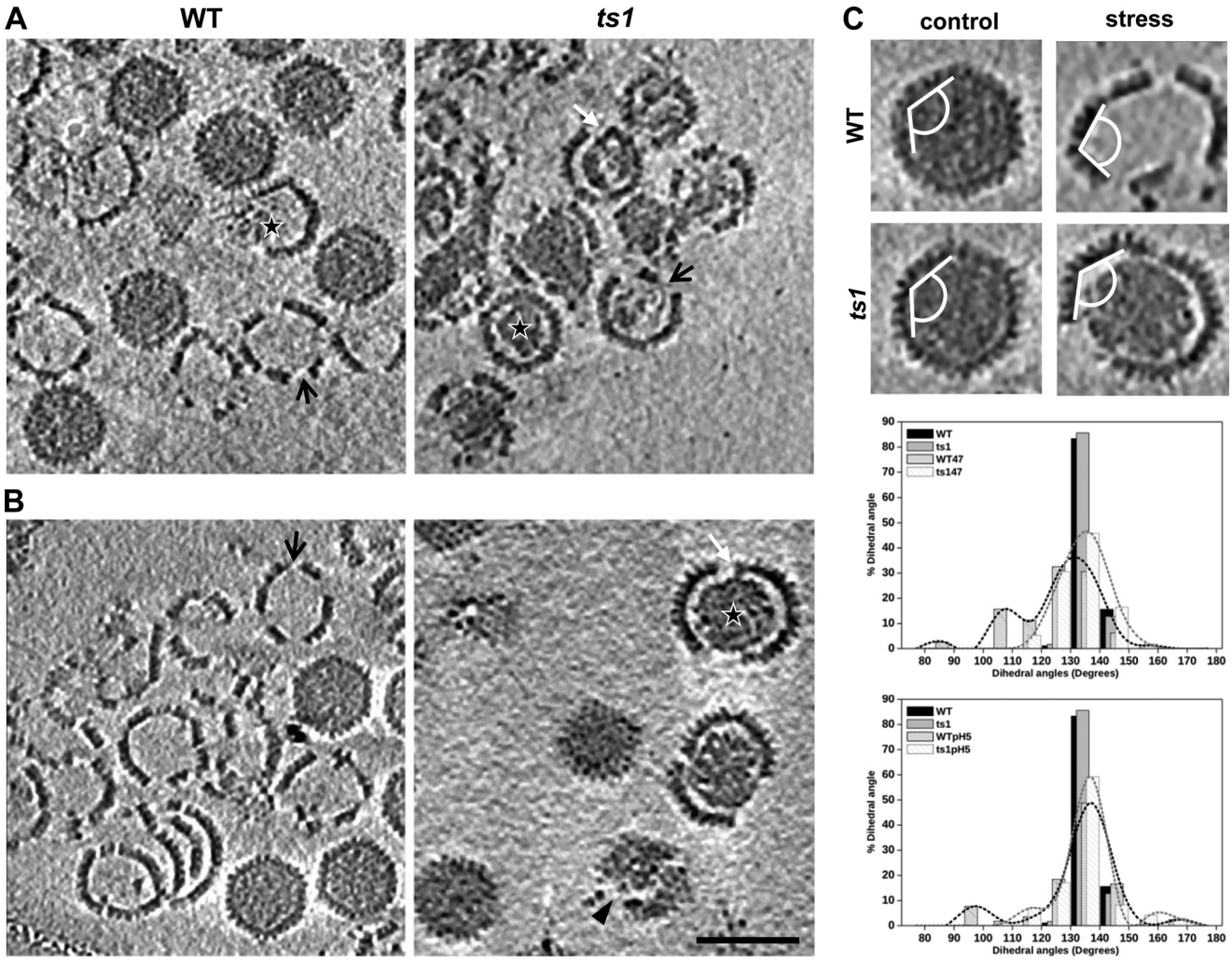

FIGURE 4. **Cryoelectron tomography analysis of structural changes induced by high stress.** *A,* representative sections of tomograms showing WT and *ts1* virus at 47 °C; *B,* at pH 5. The *bar* represents 100 nm. *Black arrows* indicate missing GOSs; *stars* indicate core remnants in open capsids; *white arrows* indicate capsid-core contacts; *black arrowhead* indicates a tangential view of a capsid crack. *C,* analysis of capsid curvature. *Top panel,* schematics showing examples of dihedral angles on central sections of individual virus tomograms. *Middle* and *bottom panels,* histograms of angle values for WT and *ts1* control, intact virions; and for disrupted capsids at 47 °C or pH 5.

TABLE 5

Statistics of dihedral angles in disrupted capsids under high stress

A total of 30 individual virus tomograms were examined for each condition. The number of angle measurements n for each case is indicated.

Condition	WT	*ts1*
Perfect icosahedron	138°	138°
Control	137 ± 3° (n = 180)	136 ± 3° (n = 180)
47 °C	125 ± 13° (n = 160)	133 ± 8° (n = 170)
pH 5	132 ± 14° (n = 168)	134 ± 11° (n = 169)

particles were aligned and averaged, radial profiles indicated that the WT core density had decreased not only in the periphery but also in the center of the virion, *i.e.* core relaxation or component loss increased with increasing stress levels. Conversely, core density in *ts1* virions lacking some pentons remained unaltered, even at pH 5 or 47 °C (supplemental Fig. S4).

Mechanical Capsid Disruption—AFM nanoindentation assays allow exploring virus stability under mechanical stress. After locating an individual intact virus on the surface (Fig. 5*A*), the cantilever pushes the virion at the very top of the particle. Cantilever bending is recorded as a function of *z* displacement, thus eliciting the virus deformation as a function of the vertical force (48). During the first stages of indentation, the virus particles undergo a linear deformation that is reflected by a sustained climbing in the force indentation curve (Fig. 5, *C* and *D*) and provides the spring constant of the virus k_v (49). At a certain point, the curve tendency sharply changes, and the force suddenly starts decreasing due to capsid failure. The point where tendency changes determines the breaking force. Finally, an image of the virus is taken to confirm its disruption (Fig. 5*B*). In the experimental conditions used here, viruses preferentially attached to the mica in a 3-fold orientation.

We recorded data from single nanoindentations on 25 WT (Fig. 5*C*) and 28 *ts1* (Fig. 5*D*) particles. From the results obtained in conditions of thermal or chemical stress, we would have expected to find the mature capsid more fragile and softer than the immature one. On the contrary, WT virions presented both higher breaking force (3.3 ± 0.2 nN) and stiffness (0.46 ± 0.02 N/m) than *ts1* particles (2.3 ± 0.2 nN and 0.38 ± 0.04 N/m). Further analysis of indentation curves can supply extra information about the core. From the experimental curves in

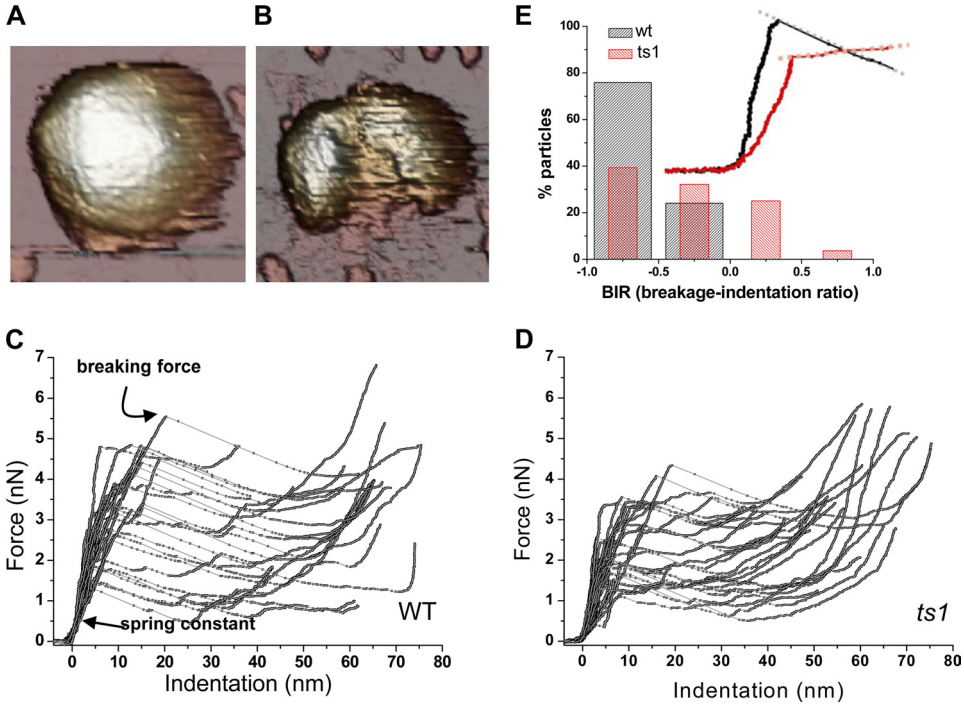

FIGURE 5. **Mechanical capsid disruption.** *A,* intact adenovirus AFM image. *B,* same virion as in *A* after disruption by a single nanoindentation. *C,* indentation data corresponding to 25 WT virions. *Arrows* indicate the curve spots for calculating the particle stiffness and the breaking force. *D,* indentation data corresponding to 28 *ts1* particles. *E,* BIR histogram of immature (*red*) and mature (*black*) virions. The *inset* shows two example indentation curves (WT in *black*, *ts1* in *red*) and the region used for the calculation of BIR (*dotted lines*).

Fig. 5, *C* and *D*, the total indentation found for adenovirus was equal to or greater than 40 nm, which is about half the capsid diameter. Taking into account this depth, and the particle topography after indentation (Fig. 5*B*), it is clear that the tip penetrates the virus core. Therefore, the quantitative analysis of the abrupt decay of the force beyond capsid breakage (*inset* in Fig. 5*E*) provides information about core fraying. Converting back the force (*y* axes of Fig. 5, *C* and *D*) to cantilever deflection (nm), we estimated the cantilever bending during post-failure indentation by calculating the slope from the breakage point to 40 nm of indentation, and we called this dimensionless magnitude breakage-indentation ratio (BIR). The more negative the BIR, the faster the core is penetrated by the tip in free fall once the capsid is broken. The classification of BIR in histograms for both mature and immature virions (Fig. 5*E*) shows that WT particles yield faster than *ts1* ones, which even show BIR-positive values. This finding provides direct physical evidence of the higher resilience of the immature core, while mature cores unravel more easily when pushed by the AFM tip.

DISCUSSION

Adenovirus maturation and uncoating have been extensively explored for several decades. Elegant biophysics, cellular and molecular biology studies have given insight into the maturation process on the one hand (22, 26, 50) and the sequential uncoating on the other hand (8, 9, 12, 13). The entry defect of *ts1* had previously been related with increased stability (5, 8, 51). However, the structural and physical determinants conferring extra stability to the immature virion had not been characterized in detail nor had the structural changes undergone during uncoating been observed at single virion levels in three-dimensional maps. Therefore, the results presented here help to elucidate the role of proteolytic maturation in adenovirus assembly and uncoating.

Implications for Assembly—Among the dsDNA viruses, maturation energetics are best understood for bacteriophage P22 and HK97 (52, 53). In both cases, large conformational rearrangements accompany a progressive stabilization of the virus particle. In contrast, adenovirus maturation is not accompanied by large structural rearrangements (4, 5). Now we show that, in contrast to the bacteriophage case, the immature adenovirus particle is more stable than the mature one under a variety of stress conditions. To our knowledge, this is the first case reported of a virus assembly intermediate more stable than the final, infectious product.

What makes the immature virion highly stable? The three thermal transitions detected by DSC during capsid disruption take place at lower temperatures in WT than in *ts1* virus, suggesting a role of protein maturation in virus stabilization. None of these transitions was observed in purified hexon denaturation (42). They may therefore arise from disruption of interactions between hexons in the assembled virion or from denaturation of other proteins present at high enough concentration to be detected. If this were the case, pVII and pVI, followed by pIIIa, penton base, IX, pVIII, and fiber protein (in this particular order), would be the most probable candidates, taking into account their respective contributions to the total protein content. Interestingly, four out of the six candidates, and notably the two most abundant, pVII and pVI, are processed by the virus protease and participate in capsid and core interactions that are affected during virus maturation (5). In addition, by

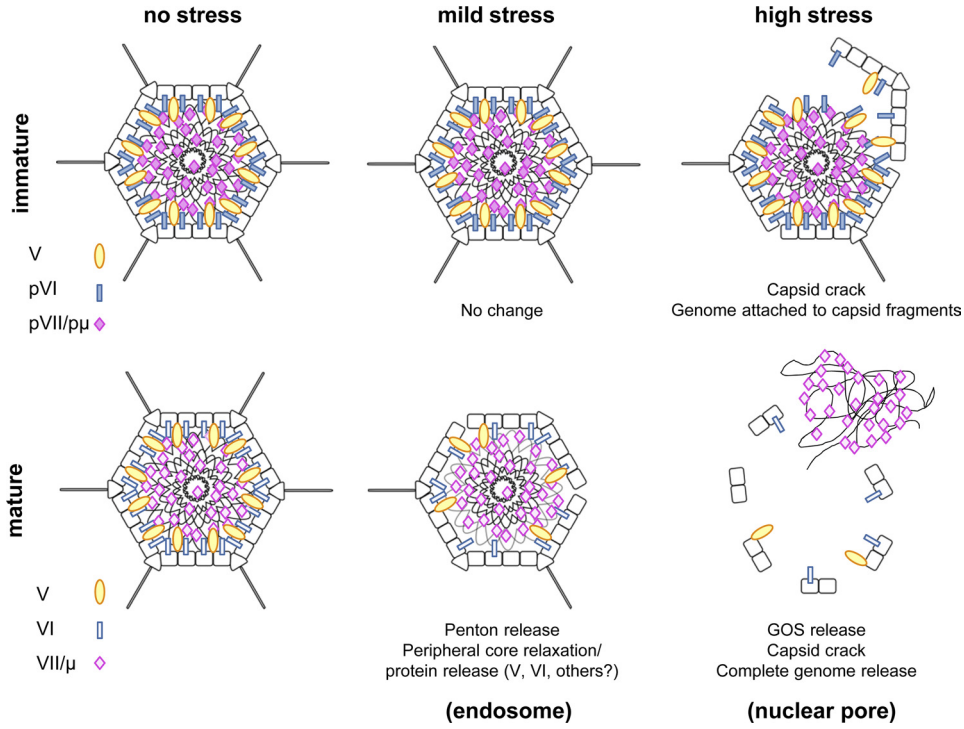

FIGURE 6. **Schematic depicting the stages of mature and immature adenovirus disruption by acidification.** For the mature virion, cellular compartments where similar disassembly events are likely to occur are indicated in *parentheses*.

sequence modification, proteolytic maturation might directly affect protein intrinsic stability but also indirect stabilization through available intermolecular interactions. Both effects could explain the differences found in the T_m values of transitions leading to virion disassembly and would reinforce the role of precursors as scaffold elements, involved in energetically stabilizing the assembly intermediates and increasing the chances of assembly. A similar process has been described in bacteriophage HK97, where the coat protein Δ-domain acts as a scaffold to promote procapsid assembly and then is processed by the virus protease allowing the transition to the next assembly intermediate (54).

We have previously shown that the presence of capsid (pIIIa, pVI, and pVIII) and core (pVII and pre-μ) precursor proteins results in additional ordered interactions in the virus shell and core (5). Here, we show the effect of these extra interactions. First, immature particles are resistant to the loss of pentons, under conditions in which mature virions readily release them (*e.g.* 40 °C, pH 6). This difference indicates a role for the precursor proteins in preventing premature vertex release, particularly during the DNA packaging process. The need to reinforce vertex structures during morphogenesis has previously been hypothesized in other icosahedral viruses (55).

A second aspect of immature adenovirus stabilization is that interactions maintaining the capsid curvature are preserved, even after losing complete vertex structures, including penton and peripentonal hexons (GOS). In the third place, the immature adenovirus core is a tightly compacted sphere that remains bound to capsid fragments even in high stress conditions. Notably, precursor protein pVI, located at the inner surface the icosahedral shell, binds both hexon and DNA (56, 57). All these observations indicate that the interactions established by precursor proteins, whether in the capsid or between capsid and core (*e.g.* pVI), may play a role in establishing and reinforcing correct capsid curvature during assembly.

Implications for Uncoating—A second role of the maturation process is preparing the virus particle for genome release. On entering the new host cell, virions have to fall apart in a concerted way so that their genome is uncoated at the appropriate place and time to start a new productive virus cycle. Here, we show how maturation prepares adenovirus for proper uncoating and what structural changes are undergone by the virion during disruption, particularly at moderately acidic conditions mimicking those in the early endosome.

Unlike the bacteriophage capsids, the mature adenovirus virion does not represent a global energy minimum in the assembly pathway. It is rather a metastable particle, primed for sequential disassembly through a series of irreversible events and massive genome exposure under the appropriate conditions. These energetic differences are likely related to the different infection mechanisms used by bacteriophage and adenovirus. dsDNA bacteriophage translocate their genomes into the host cell leaving the protein shell behind (58), whereas adenovirus is engulfed by the cell and disassembles within to expose its genome to the cell nucleus machinery (59). In this sense, adenovirus is similar to other nonenveloped animal viruses, such as poliovirus, where interaction with the receptor is the trigger to start the cascade of structural changes leading to uncoating (60).

The pathway of capsid dismantling is schematically depicted in Fig. 6. Mature adenovirus uncoating starts by releasing pentons. This was expected, because theoretical models of icosahedral virus capsids predict that vertex capsomers experience higher levels of stress simply due to capsid geometry. They have

fewer interactions, because of having only five and not six neighbors, which makes them the first elements to be lost upon disturbances in the system (47). Furthermore, penton loss had already been shown by assays following the fate of different virus proteins upon cell entry (9, 10). Our cryoelectron tomography images show for the first time how this happens in single virions. In mild stress conditions, some pentons are released but not all. In particular, mild acidification resulted in the release of only one or two pentons per virion. Initial penton release was not accompanied by loss of other capsomers in the GOS; nor does acidification *per se* result in fiber release. These observations are in agreement with the hypothesis that an interaction with integrin and a concomitant structural change in penton base are needed for fiber release (11, 61).

Penton loss is accompanied by loss of density in the peripheral core regions and, in the case of mild acidification, a massive increase in DNA accessibility to intercalating dyes. Neither pentons nor peripheral core components were released from immature *ts1* particles under mild stress. Loss of peripheral core material is consistent with previous observations indicating release of some internal components in the early endosome, such as core polypeptide V and, more critically, the membrane disrupting polypeptide VI (12, 13). Both V and VI are thought to occupy positions bridging the internal capsid surface to the core (4, 5, 62). Other candidates to be released from slightly disrupted WT capsids are the small peptides resulting from AVP cleavages. DNA accessibility in these conditions results from penton defects and core reorganization but not from core ejection, as all virions observed still retained electron dense contents, and only very rarely were short dsDNA stretches observed protruding from the virions. These properties correlate with the need for the partially disassembled virion to keep protecting its genome while trafficking in the cytosol until arrival to the nuclear pore, while at the same time allowing access to cellular sensors triggering inflammatory responses (15).

Higher levels of stress in mature virions result in release of peripentonal hexons, deviations from icosahedral curvature, capsids cracking open, and complete core ejection. As described above, maturation allows for larger variations in capsid curvature and is crucial for relaxing the core organization and facilitating its separation from the disrupted capsid. Theoretical models predict icosahedral capsid burst by cracks running across hexameric positions when protein-protein interactions between capsomers are weakened, for example by swelling, an increase in internal pressure, or curvature changes in general (47). We therefore hypothesize that, although adenovirus does not undergo the large conformational swelling transitions observed in other viruses, a small degree of swelling or an increase in internal pressure may be part of the virus uncoating process.

A Role for Internal Pressure in Adenovirus Priming for Uncoating—Nanoindentation assays using AFM in physiological conditions have lately provided insights into the mechanical properties of virus capsids. Usually, mechanical strength and stiffness are considered a signature of virus stability (63–65), *i.e.* the harder the virus, the more resilient to aggressive conditions. However, this may not necessarily be the case, because stiffness does not guarantee that a virus can survive in hostile chemical or thermal environments. This is the kind of behavior we find for adenovirus; immature *ts1*, which withstands higher levels of thermal or chemical stress than WT, is softer and breaks at lower forces than WT when indented with the AFM tip. Conversely, the metastable WT virions appear mechanically stronger (breaking at higher forces) and stiffer. Thus, in adenovirus, mechanical stability does not correlate with thermal or chemical stability.

The adenovirus mature capsid is brittle and stiff, and its pentons are more prone to come off than those in the elastic immature particle. Maturation drastically changes the core organization and reduces interactions that kept the DNA tightly condensed. The relationship between these observations points to the possibility that relaxation of the core upon maturation increases the internal pressure in the virion. The adenovirus capsid is usually thought to be pressurized, by analogy with other dsDNA viruses (66). However, the case of adenovirus is different from that of bacteriophage, because the dsDNA genome is forming a complex with a large quantity of charge-neutralizing proteins. No direct estimations of the internal pressure in adenovirus are available so far.

Based on the results presented here, we hypothesize that an increase in internal pressure resulting from proteolytic maturation of the charge-screening core polypeptides pVII and pre-μ is a determinant in priming adenovirus capsid for stepwise uncoating. This increase, together with severing of capsid-core contacts via the precursor proteins (particularly pVI), would facilitate release of pentons and peripheral core material, followed by capsid deformation, cracking, and complete ejection of the genetic material to achieve virus propagation and therefore infectivity.

Acknowledgments—We are grateful to María López (Centro Nacional de Biotecnología) for expert technical help; Dr. Juan Fontana (NIAMS, National Institutes of Health) for help with cryoelectron tomography; and Drs. D. T. Curiel and I. P. Dmitriev (Washington University School of Medicine; St. Louis) for the initial seed to propagate Ad5GL. CIBERES is an initiative of the Instituto de Salud Carlos III of Spain.

REFERENCES

1. Leen, A. M., and Rooney, C. M. (2005) Adenovirus as an emerging pathogen in immunocompromised patients. *Br. J. Haematol.* **128,** 135–144
2. Singh, R., and Kostarelos, K. (2009) Designer adenoviruses for nanomedicine and nanodiagnostics. *Trends Biotechnol.* **27,** 220–229
3. Liu, H., Jin, L., Koh, S. B., Atanasov, I., Schein, S., Wu, L., and Zhou, Z. H. (2010) Atomic structure of human adenovirus by cryo-EM reveals interactions among protein networks. *Science* **329,** 1038–1043
4. Silvestry, M., Lindert, S., Smith, J. G., Maier, O., Wiethoff, C. M., Nemerow, G. R., and Stewart, P. L. (2009) Cryoelectron microscopy structure of adenovirus type 2 temperature-sensitive mutant 1 reveals insight into the cell entry defect. *J. Virol.* **83,** 7375–7383
5. Pérez-Berná, A. J., Marabini, R., Scheres, S. H., Menéndez-Conejero, R., Dmitriev, I. P., Curiel, D. T., Mangel, W. F., Flint, S. J., and San Martín, C. (2009) Structure and uncoating of immature adenovirus. *J. Mol. Biol.* **392,** 547–557
6. Baniecki, M. L., McGrath, W. J., McWhirter, S. M., Li, C., Toledo, D. L., Pellicena, P., Barnard, D. L., Thorn, K. S., and Mangel, W. F. (2001) Interaction of the human adenovirus proteinase with its 11-amino acid cofac-

tor pVIc. *Biochemistry* **40,** 12349–12356
7. Chroboczek, J., Bieber, F., and Jacrot, B. (1992) The sequence of the genome of adenovirus type 5 and its comparison with the genome of adenovirus type 2. *Virology* **186,** 280–285
8. Smith, J. G., Wiethoff, C. M., Stewart, P. L., and Nemerow, G. R. (2010) Adenovirus. *Curr. Top. Microbiol. Immunol.* **343,** 195–224
9. Greber, U. F., Willetts, M., Webster, P., and Helenius, A. (1993) Stepwise dismantling of adenovirus 2 during entry into cells. *Cell* **75,** 477–486
10. Nakano, M. Y., Boucke, K., Suomalainen, M., Stidwill, R. P., and Greber, U. F. (2000) The first step of adenovirus type 2 disassembly occurs at the cell surface, independently of endocytosis and escape to the cytosol. *J. Virol.* **74,** 7085–7095
11. Lindert, S., Silvestry, M., Mullen, T. M., Nemerow, G. R., and Stewart, P. L. (2009) Cryoelectron microscopy structure of an adenovirus-integrin complex indicates conformational changes in both penton base and integrin. *J. Virol.* **83,** 11491–11501
12. Puntener, D., Engelke, M. F., Ruzsics, Z., Strunze, S., Wilhelm, C., and Greber, U. F. (2011) Stepwise loss of fluorescent core protein V from human adenovirus during entry into cells. *J. Virol.* **85,** 481–496
13. Wiethoff, C. M., Wodrich, H., Gerace, L., and Nemerow, G. R. (2005) Adenovirus protein VI mediates membrane disruption following capsid disassembly. *J. Virol.* **79,** 1992–2000
14. Gastaldelli, M., Imelli, N., Boucke, K., Amstutz, B., Meier, O., and Greber, U. F. (2008) Infectious adenovirus type 2 transport through early but not late endosomes. *Traffic* **9,** 2265–2278
15. Nociari, M., Ocheretina, O., Schoggins, J. W., and Falck-Pedersen, E. (2007) Sensing infection by adenovirus. Toll-like receptor-independent viral DNA recognition signals activation of the interferon regulatory factor 3 master regulator. *J. Virol.* **81,** 4145–4157
16. Bremner, K. H., Scherer, J., Yi, J., Vershinin, M., Gross, S. P., and Vallee, R. B. (2009) Adenovirus transport via direct interaction of cytoplasmic dynein with the viral capsid hexon subunit. *Cell Host Microbe* **6,** 523–535
17. Suomalainen, M., Nakano, M. Y., Keller, S., Boucke, K., Stidwill, R. P., and Greber, U. F. (1999) Microtubule-dependent plus- and minus end-directed motilities are competing processes for nuclear targeting of adenovirus. *J. Cell Biol.* **144,** 657–672
18. Chatterjee, P. K., Vayda, M. E., and Flint, S. J. (1986) Adenoviral protein VII packages intracellular viral DNA throughout the early phase of infection. *EMBO J.* **5,** 1633–1644
19. Greber, U. F., Webster, P., Weber, J., and Helenius, A. (1996) The role of the adenovirus protease on virus entry into cells. *EMBO J.* **15,** 1766–1777
20. Greber, U. F., Suomalainen, M., Stidwill, R. P., Boucke, K., Ebersold, M. W., and Helenius, A. (1997) The role of the nuclear pore complex in adenovirus DNA entry. *EMBO J.* **16,** 5998–6007
21. Trotman, L. C., Mosberger, N., Fornerod, M., Stidwill, R. P., and Greber, U. F. (2001) Import of adenovirus DNA involves the nuclear pore complex receptor CAN/Nup214 and histone H1. *Nat. Cell Biol.* **3,** 1092–1100
22. Weber, J. M. (1999) in *Adenoviruses: Basic Biology to Gene Therapy* (Seth, P., ed) pp. 79–83, R. G. Landes, Austin, TX
23. Weber, J. (1976) Genetic analysis of adenovirus type 2 III. Temperature sensitivity of processing viral proteins. *J. Virol.* **17,** 462–471
24. Rancourt, C., Keyvani-Amineh, H., Sircar, S., Labrecque, P., and Weber, J. M. (1995) Proline 137 is critical for adenovirus protease encapsidation and activation but not enzyme activity. *Virology* **209,** 167–173
25. Cotten, M., and Weber, J. M. (1995) The adenovirus protease is required for virus entry into host cells. *Virology* **213,** 494–502
26. San Martín, C. (2012) Latest insights on adenovirus structure and assembly. *Viruses* **4,** 847–877
27. Seki, T., Dmitriev, I., Kashentseva, E., Takayama, K., Rots, M., Suzuki, K., and Curiel, D. T. (2002) Artificial extension of the adenovirus fiber shaft inhibits infectivity in coxsackievirus and adenovirus receptor-positive cell lines. *J. Virol.* **76,** 1100–1108
28. Sanchez-Ruiz, J. M. (1992) Theoretical analysis of Lumry-Eyring models in differential scanning calorimetry. *Biophys. J.* **61,** 921–935
29. Carreira, A., Menéndez, M., Reguera, J., Almendral, J. M., and Mateu, M. G. (2004) *In vitro* disassembly of a parvovirus capsid and effect on capsid stability of heterologous peptide insertions in surface loops. *J. Biol. Chem.* **279,** 6517–6525
30. Harris, A., Cardone, G., Winkler, D. C., Heymann, J. B., Brecher, M., White, J. M., and Steven, A. C. (2006) Influenza virus pleiomorphy characterized by cryoelectron tomography. *Proc. Natl. Acad. Sci. U.S.A.* **103,** 19123–19127
31. Mastronarde, D. N. (2005) Automated electron microscope tomography using robust prediction of specimen movements. *J. Struct. Biol.* **152,** 36–51
32. Kremer, J. R., Mastronarde, D. N., and McIntosh, J. R. (1996) Computer visualization of three-dimensional image data using IMOD. *J. Struct. Biol.* **116,** 71–76
33. Agulleiro, J. I., and Fernandez, J. J. (2011) Fast tomographic reconstruction on multicore computers. *Bioinformatics* **27,** 582–583
34. Frangakis, A. S., and Hegerl, R. (2001) Noise reduction in electron tomographic reconstructions using nonlinear anisotropic diffusion. *J. Struct. Biol.* **135,** 239–250
35. Heymann, J. B., Cardone, G., Winkler, D. C., and Steven, A. C. (2008) Computational resources for cryoelectron tomography in Bsoft. *J. Struct. Biol.* **161,** 232–242
36. Scheres, S. H., Núñez-Ramírez, R., Sorzano, C. O., Carazo, J. M., and Marabini, R. (2008) Image processing for electron microscopy single-particle analysis using XMIPP. *Nat. Protoc.* **3,** 977–990
37. Scheres, S. H., Melero, R., Valle, M., and Carazo, J. M. (2009) Averaging of electron subtomograms and random conical tilt reconstructions through likelihood optimization. *Structure* **17,** 1563–1572
38. Ortega-Esteban, A., Horcas, I., Hernando-Pérez, M., Ares, P., Pérez-Berná, A. J., San Martín, C., Carrascosa, J. L., de Pablo, P. J., and Gómez-Herrero, J. (2012) Minimizing tip-sample forces in jumping mode atomic force microscopy in liquid. *Ultramicroscopy* **114,** 56–61
39. Sader, J. E., Chon, J. W., and Mulvaney, P. (1999) Calibration of rectangular atomic force microscope cantilevers. *Rev. Sci. Instrum.* **70,** 3967–3969
40. Zink, M., and Grubmüller, H. (2009) Mechanical properties of the icosahedral shell of southern bean mosaic virus. A molecular dynamics study. *Biophys. J.* **96,** 1350–1363
41. Horcas, I., Fernández, R., Gómez-Rodríguez, J. M., Colchero, J., Gómez-Herrero, J., and Baro, A. M. (2007) WSXM. A software for scanning probe microscopy and a tool for nanotechnology. *Rev. Sci. Instrum.* **78,** 013705
42. Ihnat, P. M., Vellekamp, G., Obenauer-Kutner, L. J., Duan, J., Han, M. A., Witchey-Lakshmanan, L. C., and Grace, M. J. (2005) Comparative thermal stabilities of recombinant adenoviruses and hexon protein. *Biochim. Biophys. Acta* **1726,** 138–151
43. Rexroad, J., Evans, R. K., and Middaugh, C. R. (2006) Effect of pH and ionic strength on the physical stability of adenovirus type 5. *J. Pharm. Sci.* **95,** 237–247
44. Rexroad, J., Martin, T. T., McNeilly, D., Godwin, S., and Middaugh, C. R. (2006) Thermal stability of adenovirus type 2 as a function of pH. *J. Pharm. Sci.* **95,** 1469–1479
45. Rexroad, J., Wiethoff, C. M., Green, A. P., Kierstead, T. D., Scott, M. O., and Middaugh, C. R. (2003) Structural stability of adenovirus type 5. *J. Pharm. Sci.* **92,** 665–678
46. Lozach, P. Y., Huotari, J., and Helenius, A. (2011) Late-penetrating viruses. *Curr. Opin. Virol.* **1,** 35–43
47. Zandi, R., and Reguera, D. (2005) Mechanical properties of viral capsids. *Phys. Rev. E Stat. Nonlin. Soft. Matter Phys.* **72,** 021917
48. De Pablo, P. J., Schaap, I. A., MacKintosh, F. C., and Schmidt, C. F. (2003) Deformation and collapse of microtubules on the nanometer scale. *Phys. Rev. Lett.* **91,** 981011–981014
49. Carrasco, C., Carreira, A., Schaap, I. A., Serena, P. A., Gómez-Herrero, J., Mateu, M. G., and de Pablo, P. J. (2006) DNA-mediated anisotropic mechanical reinforcement of a virus. *Proc. Natl. Acad. Sci. U.S.A.* **103,** 13706–13711
50. Mangel, W. F., McGrath, W. J., Toledo, D. L., and Anderson, C. W. (1993) Viral DNA and a viral peptide can act as cofactors of adenovirus virion proteinase activity. *Nature* **361,** 274–275
51. Hannan, C., Raptis, L. H., Déry, C. V., and Weber, J. (1983) Biological and structural studies with an adenovirus type 2 temperature-sensitive mutant defective for uncoating. *Intervirology* **19,** 213–223
52. Galisteo, M. L., and King, J. (1993) Conformational transformations in the protein lattice of phage P22 procapsids. *Biophys. J.* **65,** 227–235

53. Ross, P. D., Conway, J. F., Cheng, N., Dierkes, L., Firek, B. A., Hendrix, R. W., Steven, A. C., and Duda, R. L. (2006) A free energy cascade with locks drives assembly and maturation of bacteriophage HK97 capsid. *J. Mol. Biol.* **364,** 512–525
54. Huang, R. K., Khayat, R., Lee, K. K., Gertsman, I., Duda, R. L., Hendrix, R. W., and Johnson, J. E. (2011) The Prohead-I structure of bacteriophage HK97. Implications for scaffold-mediated control of particle assembly and maturation. *J. Mol. Biol.* **408,** 541–554
55. Teschke, C. M., McGough, A., and Thuman-Commike, P. A. (2003) Penton release from P22 heat-expanded capsids suggests importance of stabilizing penton-hexon interactions during capsid maturation. *Biophys. J.* **84,** 2585–2592
56. Wodrich, H., Guan, T., Cingolani, G., Von Seggern, D., Nemerow, G., and Gerace, L. (2003) Switch from capsid protein import to adenovirus assembly by cleavage of nuclear transport signals. *EMBO J.* **22,** 6245–6255
57. Russell, W. C., and Precious, B. (1982) Nucleic acid-binding properties of adenovirus structural polypeptides. *J. Gen. Virol.* **63,** 69–79
58. Johnson, J. E., and Chiu, W. (2007) DNA packaging and delivery machines in tailed bacteriophages. *Curr. Opin. Struct. Biol.* **17,** 237–243
59. Strunze, S., Engelke, M. F., Wang, I. H., Puntener, D., Boucke, K., Schleich, S., Way, M., Schoenenberger, P., Burckhardt, C. J., and Greber, U. F. (2011) Kinesin-1-mediated capsid disassembly and disruption of the nuclear pore complex promote virus infection. *Cell Host Microbe* **10,** 210–223
60. Hogle, J. M. (2002) Poliovirus cell entry. Common structural themes in viral cell entry pathways. *Annu. Rev. Microbiol.* **56,** 677–702
61. Burckhardt, C. J., Suomalainen, M., Schoenenberger, P., Boucke, K., Hemmi, S., and Greber, U. F. (2011) Drifting motions of the adenovirus receptor CAR and immobile integrins initiate virus uncoating and membrane lytic protein exposure. *Cell Host Microbe* **10,** 105–117
62. Chatterjee, P. K., Vayda, M. E., and Flint, S. J. (1985) Interactions among the three adenovirus core proteins. *J. Virol.* **55,** 379–386
63. Roos, W. H., Radtke, K., Kniesmeijer, E., Geertsema, H., Sodeik, B., and Wuite, G. J. (2009) Scaffold expulsion and genome packaging trigger stabilization of herpes simplex virus capsids. *Proc. Natl. Acad. Sci. U.S.A.* **106,** 9673–9678
64. Baclayon, M., Shoemaker, G. K., Uetrecht, C., Crawford, S. E., Estes, M. K., Prasad, B. V., Heck, A. J., Wuite, G. J., and Roos, W. H. (2011) Prestress strengthens the shell of Norwalk virus nanoparticles. *Nano. Lett.* **11,** 4865–4869
65. Roos, W. H., Gertsman, I., May, E. R., Brooks, C. L., 3rd, Johnson, J. E., and Wuite, G. J. (2012) Mechanics of bacteriophage maturation. *Proc. Natl. Acad. Sci. U.S.A.* **109,** 2342–2347
66. Gelbart, W. M., and Knobler, C. M. (2009) Virology. Pressurized viruses. *Science* **323,** 1682–1683

The Role of Capsid Maturation on Adenovirus Priming for Sequential Uncoating

Ana J. Pérez-Berná, Alvaro Ortega-Esteban, Rosa Menéndez-Conejero, Dennis C. Winkler, Margarita Menéndez, Alasdair C. Steven, S. Jane Flint, Pedro J. de Pablo and Carmen San Martín

J. Biol. Chem. 2012, 287:31582-31595.
doi: 10.1074/jbc.M112.389957 originally published online July 12, 2012
